

Strong Light-Matter Interactions in Heterostructures of Atomically Thin Films

L. Britnell,¹ R. M. Ribeiro,^{2,3} A. Eckmann,⁴ R. Jalil,⁵ B. D. Belle,⁵ A. Mishchenko,¹ Y.-J. Kim,^{1,6} R. V. Gorbachev,¹ T. Georgiou,¹ S. V. Morozov,⁷ A. N. Grigorenko,¹ A. K. Geim,⁵ C. Casiraghi,^{4,8} A. H. Castro Neto,^{2,*†} K. S. Novoselov¹

The isolation of various two-dimensional (2D) materials, and the possibility to combine them in vertical stacks, has created a new paradigm in materials science: heterostructures based on 2D crystals. Such a concept has already proven fruitful for a number of electronic applications in the area of ultrathin and flexible devices. Here, we expand the range of such structures to photoactive ones by using semiconducting transition metal dichalcogenides (TMDCs)/graphene stacks. Van Hove singularities in the electronic density of states of TMDC guarantees enhanced light-matter interactions, leading to enhanced photon absorption and electron-hole creation (which are collected in transparent graphene electrodes). This allows development of extremely efficient flexible photovoltaic devices with photoresponsivity above 0.1 ampere per watt (corresponding to an external quantum efficiency of above 30%).

The advent of graphene (1) and the subsequent discovery of its multitude of superior properties (2–5) has led to the identification of many other two-dimensional (2D) crystals (6) through both chemical modification of graphene and exfoliation of other layered compounds. This new area of research and progress in precise transfer of the crystals while maintaining their quality (7, 8) has resulted in the emergence of a new class of materials: heterostructures based on 2D atomic crystals (5, 8, 9). More specifically, there is the possibility to create hybrid materials by stacking combinations of 2D crystals with differing properties. These structures are interesting from both fundamental and application points of view. It has, for instance, been shown that layering sheets of graphene and hexagonal boron nitride (hBN), molybdenum disulfide (MoS₂), or tungsten disulfide (WS₂) allows operation of tunneling transistors (9, 10) and permitted the observation of phenomena such as Coulomb drag (11) and the fractional quantum Hall effect (12).

Many other crystals have been found to exfoliate to monolayer by both mechanical (6) and chemical methods (13). Transition metal dichalcogenides (TMDCs) are a group of layered ma-

terials that has attracted a lot of interest (14). They are structured such that each layer consists of three atomic planes: a triangular lattice of transition metal atoms sandwiched between two triangular lattices of chalcogen atoms (S, Se, or Te). There is strong covalent bonding between the atoms within each layer and predominantly weak

van der Waals bonding between adjacent layers. Many of these materials—NbSe₂, MoS₂, WS₂, and TaS₂, to name a few—are structurally similar but have an array of electronic properties ranging from semiconducting (15) to metallic (16), from charge density waves to superconducting (17), depending on their exact composition, electronic density, geometry, and thickness (18).

Besides the traditional applications of TMDC films as solid-state lubricants and industrial surface protection (19, 20), films of these materials have long been considered for photovoltaic devices, due to their large optical absorption, which is greater than 10⁷ m⁻¹ across the visible range, meaning that 95% of the light can be absorbed by a 300-nm film. A further advantage of WS₂ is its chemical stability (21, 22) and band gaps in the visible part of the spectrum (22–24).

Previously, planar WS₂ (21) and MoS₂ (22) structures were studied for photovoltaic applications. However, efforts to extract photocurrent have been hampered by the need to create a p-n junction to separate the electron-hole (e-h) pairs created by incoming photons. Here, we show that, with the arrival of vertical 2D-crystal-based heterostructures, a beneficial combination of each material's properties emerges: TMDCs as good photoactive materials and graphene as a good transparent electrode. Using a Gr/TMDC/Gr stack (here, Gr stands for graphene) with appropriately

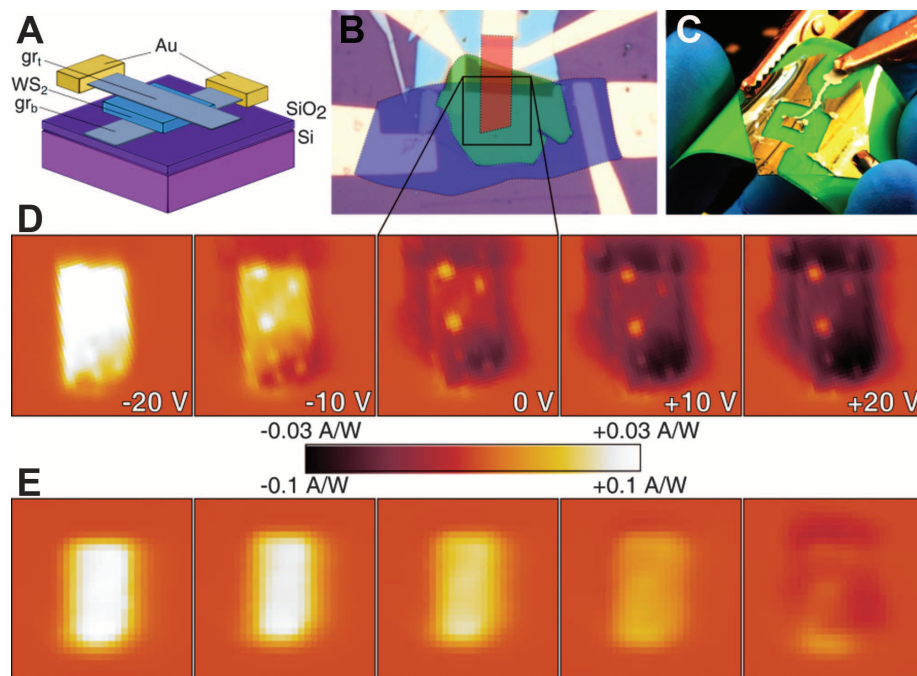


Fig. 1. Device structure and photocurrent mapping. (A) A schematic of the device with the principal layers shown. hBN is not shown. (B) An optical micrograph of one of our devices. The shading of the three constituent layers denotes the regions of the respective materials—top and bottom graphene electrodes are shown in red and blue, and WS₂ is shown in green. (C) A photograph of one of our flexible devices placed on an electroluminescent mat. (D and E) photocurrent maps taken before (D) and after (E) doping the top graphene layer with water vapor. A signal is only seen in the area where all three layers overlap. The two graphene layers were connected via a 1 k Ω resistor, on which the photocurrent was measured. No bias was applied, and for both (E) and (D), the maps were taken at gate voltages from -20 V to $+20$ V. The scale of the maps is given by their width, 20 μ m.

¹School of Physics and Astronomy, University of Manchester, Oxford Road, Manchester, M13 9PL, UK. ²Graphene Research Centre, National University of Singapore, 6 Science Drive 2, Singapore 117546. ³Departamento de Física and Centro de Física, Universidade do Minho, P-4710-057, Braga, Portugal. ⁴School of Chemistry and Photon Science Institute, University of Manchester, Oxford Road, Manchester, M13 9PL, UK. ⁵Manchester Centre for Mesoscience and Nanotechnology, University of Manchester, Oxford Road, Manchester, M13 9PL, UK. ⁶Department of Chemistry, College of Natural Sciences, Seoul National University, Seoul, 151-747, Korea. ⁷Institute for Microelectronics Technology, 142432 Chernogolovka, Russia. ⁸Department of Physics, Freie University, Berlin, 14195, Germany.

*On leave from Department of Physics, Boston University, Boston, MA, USA.

†Corresponding author. E-mail: phycast@nus.edu.sg

positioned Fermi levels and simply doping the two graphene layers differently (either by electrostatic gating or chemical methods) leads to a large photocurrent. The layered nature of our structures and exceptional mechanical strength of graphene and TMDC crystals (25, 26) also allowed us to fabricate flexible devices. Without illumination, such devices act as tunneling transistors (9, 10).

Although we concentrate the experimental data on the properties of Gr/WS₂/Gr heterostructures, our results are generic for a large class of systems where semiconducting TMDCs are the key element [see (27) for other examples of Gr/TMDC/Gr heterostructures].

Our devices comprise three principal elements—top and bottom graphene electrode layers (both micromechanically cleaved and chemical vapor deposition (CVD)-grown graphene were tested), sandwiching a photoactive TMDC layer (Fig. 1). In the fabrication procedure, the flakes were transferred with the “dry transfer” technique (in the case of micromechanically cleaved graphene) (7, 8) with thorough annealing (27) at each stage to ensure minimal contamination between the layers (28) and low-level doping of the graphene layers. We also chose to use hBN as both a substrate and an encapsulating layer to achieve a higher doping homogeneity (7, 29). Thus, the final structure of a typical device, on top of an oxidized silicon wafer or flexible polyethylene terephthalate (PET) film, was hBN/Gr/WS₂/Gr/hBN. In the case of nonflexible devices on Si/SiO₂, the doped silicon could be used as a back gate and SiO₂/hBN (typically 300 nm of SiO₂ and 20 nm of hBN) can be used as the gate dielectric. A series of such structures was produced where the thickness of the TMDC layer was varied from ~5 to 50 nm.

The current-voltage (*I-V*) characteristics of our samples strongly depended on illumination (Fig. 2A, left axis). Without illumination, the devices displayed strongly nonlinear *I-V* curves (Fig. 2A, right axis). Comparing the two sets of *I-V* curves, there is strong contrast to when they were illuminated: The resistance drops by more than three orders of magnitude, and the curves are linear around zero bias. At higher bias (~±0.2 V), the current saturates, as the number of available charge carriers in the photoactive region becomes limited.

The photocurrent generated in our devices was mapped by scanning photocurrent microscopy, where a laser spot was scanned over the sample, and the resultant photocurrent was displayed as a function of laser spot position. Photocurrent is generated only in the region where all three principal layers overlap (Fig. 1C). The origin of the photocurrent can be explained by examining the collective band diagram. In the idealized case, the structure is symmetric (Fig. 2B) and the electrons/holes generated in TMDC (by absorption of a photon with sufficient energy) have no preferred diffusion direction and, hence, no net photocurrent is measured. However, in the presence of a built-in electric field (Fig. 2C) across the TMDC

[either due to a difference in the initial doping between the graphene sheets or by gating (9)], the e-h pairs are separated and a photocurrent measured.

Immediately after fabrication (which involves the annealing stage) in the undoped state, the devices showed a minimum in the integrated photocurrent close to zero gate voltage (V_g) (Fig. 1D). For any finite V_g (either positive or negative), the photocurrent increased proportionally to V_g but began to saturate at ~±20 V, again due to the fi-

nite number of generated charge carriers. We also intentionally doped the top graphene electrode in one of our nonencapsulated samples to become p-type by exposing it to high-concentration water vapor. The photocurrent (Fig. 1E) at zero gate voltage became finite (positive), and the response with gate voltage was shifted by ~20 V. The effect is also seen in Fig. 2A, where the intercept of the *I-V* curves is shifted due to movement of the chemical potential in graphene. Our devices also

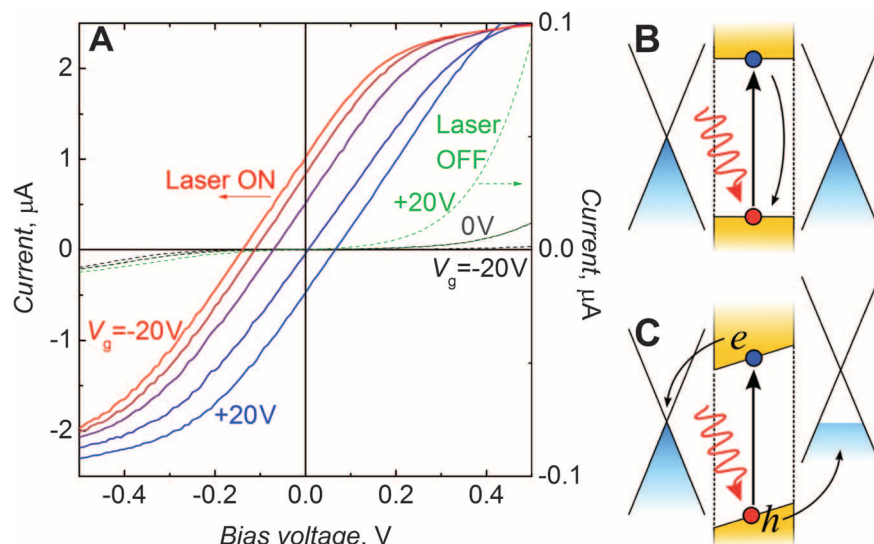
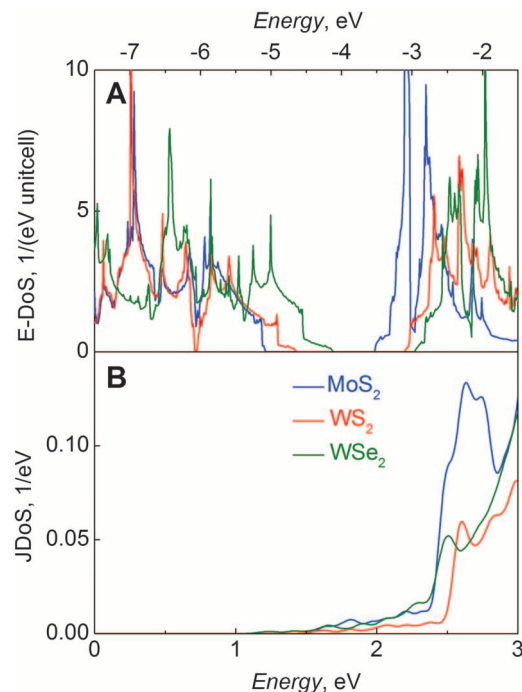


Fig. 2. Gate-dependent *I-V* characteristics. (A) (Left axis) *I-V* curves for a device on Si/SiO₂ taken under illumination at gate voltages from −20 (red) to +20 V (blue) in 10-V steps, after doping. The laser illumination energy was 2.54 eV and the power was 10 μW. The curves are linear at low bias but saturate at higher bias due to limited available charge carriers. (Right axis) *I-V* curves for the same device taken in the dark at gate voltages from −20 (black) to +20 V (green) in 20-V steps, after doping. (B and C) Schematic band diagram for Gr/WS₂/Gr heterostructure with (C) and without (B) a built-in electric field to separate the generated e-h pairs.

Fig. 3. Electronic DoS for single-layer TMDCs. (A) The DoS for monolayer TMDCs: MoS₂, WS₂, and WSe₂. Strong peaks are present in all three materials that lead to a strong light-matter interaction. (B) The JDoS with the same three TMDC materials.



showed strong gate dependence without illumination, demonstrating transistor behavior. The on/off ratio (highest to lowest current modulation) of such tunneling transistors exceeds that of previously reported devices (9). Devices made from micromechanically cleaved and CVD graphene demonstrate very similar photovoltaic and transistor behavior, opening a way for scale-up.

The photocurrent observed in these devices is surprisingly strong for only a few atomic layers of TMDC, but this strong light-matter interaction can be understood from the nature of the electronic states in this material. *Ab initio* calculations (27) for the density of states (DoS) and the joint density of states (JDoS) of three single-layer semiconducting TMDCs (WS_2 , WSe_2 , and MoS_2) show strong peaks in the visible range (Fig. 3A) associated with Van Hove singularities in the DoS. This leads to enhanced light absorption and, importantly, this is a feature that is universal to TMDCs. These Van Hove singularities come from the nature of the electronic wave functions: Whereas the valence band is essentially composed of states coming from the d orbitals of the transition metal (TM), the conduction band is characterized by a linear superposition of d orbitals of the TM and p orbitals of the chalcogen atoms. The d orbitals have a localized nature with enhanced interaction effects. The p orbitals generate the σ bands, which in turn are responsible for the structural stability

of these materials [analogous to what happens in graphene (30)]. The localized character of the electronic bands (that is, the large effective mass of the carriers) leads to the peaks—i.e., Van Hove singularities—in the DoS, which are responsible for the enhanced photoresponsivity of these materials from the nanoscopic down to atomic scale. A direct measure of the effect of the Van Hove singularities in the optical response of TMDC is given by the JDoS, defined as

$$J\text{DOS}(E) = \frac{1}{4\pi^3} \int d^3k \delta(E_{V,k} - E_{C,k} - E)$$

where V and C are the valence and conduction bands, respectively. The JDoS is a direct measure of the so-called joint critical points, that is, the Van Hove singularities in the Brillouin zone around which a photon of energy, $\hbar\omega = E_C - E_V$, is very effective in inducing electronic transitions over a relatively large region in momentum space. The large contribution to the transition probability for joint critical points gives rise to the structure observed in the frequency dependence of the optical properties of the TMDC. Thus, the photocurrent, $I(\omega)$, at some light frequency ω is proportional to $J\text{DOS}(\hbar\omega)$ (31). There is a sharp rise in the photo-absorption in the $J\text{DOS}(E)$ in the visible range of all TMDCs studied (Fig. 3B). To further confirm that our results are not dependent on the thickness of the TMDC, we calculated the

DoS and JDoS for bulk (3D) semiconducting TMDCs (27). The peaks in the DoS and the sharp rise of the JDoS are comparable with the values found for a single layer in Fig. 3B and are consistent with the previous measurements on bulk MoS_2 (32). Hence, the strong light-matter interactions in semiconducting TMDCs are not a unique feature of the bulk material and can be extended to monolayers.

The effect discussed is similar, albeit with a different physical origin, to the strong Raman absorption in 1D semiconducting carbon nanotubes. In that case, the 1D nature of the material leads to $1/\sqrt{E}$ singularities in the DoS at the top (bottom) of the valence (conduction) bands, leading also to strong light-matter response (33).

We have also computed the work function, Φ , for the semiconducting TMDCs studied here. We find that the work functions vary considerably depending on the transition metal used (for monolayer, $\Phi_{\text{WS}_2} \sim 4.6$ eV, $\Phi_{\text{WSe}_2} \sim 4.3$ eV, and $\Phi_{\text{MoS}_2} \sim 5.1$ eV) and their thickness (for bulk, $\Phi_{\text{WS}_2} \sim 4.2$ eV, $\Phi_{\text{WSe}_2} \sim 3.9$ eV, and $\Phi_{\text{MoS}_2} \sim 4.5$ eV). Notice that as the work-function of graphene is comparable in magnitude ($\Phi_G \sim 4.5$ eV), it has been shown (34) that it has a very minimal effect on the band structure of TMDC, and the Dirac point of graphene stays within the gap, facilitating efficient extraction of both electrons and holes from TMDC.

We investigated in detail the performance of our prototype photovoltaic devices. An important parameter is the extrinsic quantum efficiency (EQE), defined as the ratio of the number of charge carriers generated to the number of incident photons. This can be expressed in terms of the photocurrent I , incident power per unit area P , and excitation wavelength λ by

$$\text{EQE} = \frac{\hbar c I}{e P \lambda}$$

where h is the Planck constant, c the speed of light in vacuum, and e the electron charge. Using the relation for EQE, we calculate the efficiency (Fig. 4), where the data were collected for several wavelengths at zero bias and $V_g = -40$ V. The extrinsic quantum efficiency did not appear to be dependent on wavelength, as expected from the approximately constant optical absorption, over this range (21). It is likely that the decrease in quantum efficiency with increasing power is due to screening of the built-in electric field by the excited electrons in the conduction band of WS_2 .

The already good performance and high EQE of our devices (ensured by the peculiar band structure of TMDC used) can be further improved by optimizing light absorption in the active layer. One possible way—the use of optical resonators (35)—is already partly realized in our devices on SiO_2 , where light interference in SiO_2 layer (36, 37) enhances the optical electric field in TMDC (this is one of the reasons for better performance of our devices on SiO_2 in comparison with those on flexible substrates). Another strategy is the use of plasmonic nanostructures (38–40) or metamaterials (41). To test the idea, we applied

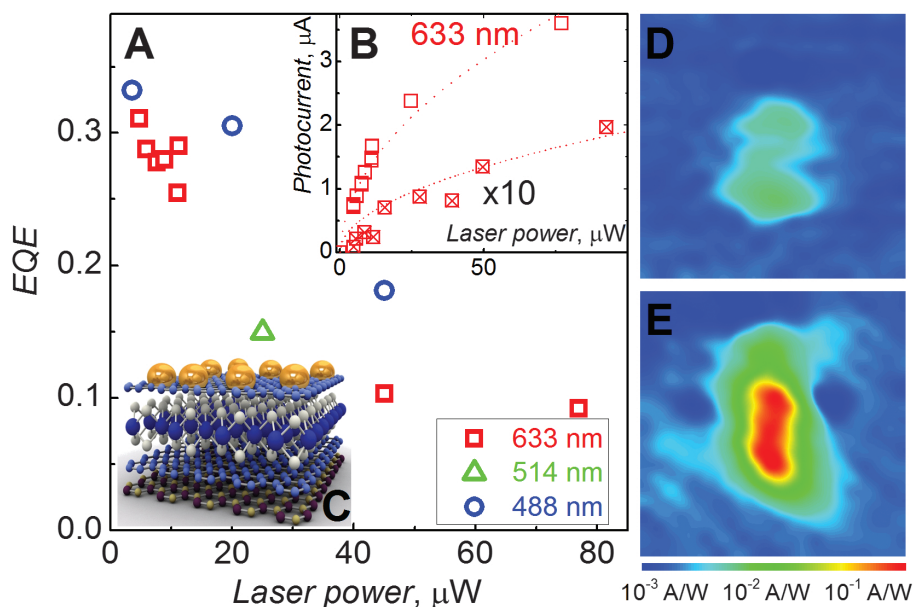


Fig. 4. Quantum efficiency. (A) The external quantum efficiency of the devices is the ratio of the number of measured e-h pairs to the number of incident photons. Due to the small variation in optical absorption across this wavelength range, the data for different wavelengths collapse onto a single curve. (B) Photocurrent measured with a 1.95-eV laser as a function of intensity; notice the sublinear dependence with laser power. This results in the largest quantum efficiency values at low intensities. Open symbols are for a device on Si/SiO_2 substrate, and crossed symbols are for a device on a flexible substrate. (C) Schematic representation of $\text{hBN}/\text{Gr}/\text{MoS}_2/\text{Gr}$ (layers bottom to top) photovoltaic device with gold nanoparticles spattered on top of the top graphene layer for plasmonic enhancement of light absorption. (D and E) Photocurrent maps of one of our $\text{hBN}/\text{Gr}/\text{MoS}_2/\text{Gr}$ devices taken before (D) and after (E) spattering of gold nanoparticles for plasmonic enhancement [illumination parameters: 633 nm, 10 μW ; scan size, 14 μm by 14 μm ; note the logarithmic scale chosen to represent the 10-fold increase in the photocurrent on (E)].

gold nanospheres (Fig. 4C) on top of one of our hBN/Gr/MoS₂/Gr heterostructures, which enhanced the optical field in the active layer and allowed for a 10-fold increase in the photocurrent, (Fig. 4, D and E) [see (27) for further details and other examples of the use of plasmonic nanostructures].

Atomically thin heterostructures of semiconducting TMDC present strong light-matter interactions that can lead to large photon absorption and photocurrent production. We are able to reach an extrinsic quantum efficiency of 30%, due to the localized character of the electronic wave functions in TMDCs that leads to large peaks in the DoS associated with van Hove singularities. The same devices demonstrate transistor behavior with on/off ratios exceeding those in previously reported devices. The use of various TMDCs, as well as their combinations, would allow one to create new transparent and flexible photonic and optoelectronic structures and devices with unique properties that surpass current technologies.

References and Notes

1. K. S. Novoselov *et al.*, *Science* **306**, 666 (2004).
2. A. K. Geim, K. S. Novoselov, *Nat. Mater.* **6**, 183 (2007).
3. A. K. Geim, *Science* **324**, 1530 (2009).
4. A. K. Geim, *Rev. Mod. Phys.* **83**, 851 (2011).
5. K. S. Novoselov, *Rev. Mod. Phys.* **83**, 837 (2011).
6. K. S. Novoselov *et al.*, *Proc. Natl. Acad. Sci. U.S.A.* **102**, 10451 (2005).
7. C. R. Dean *et al.*, *Nat. Nanotechnol.* **5**, 722 (2010).
8. L. A. Ponomarenko *et al.*, *Nat. Phys.* **7**, 958 (2011).
9. L. Britnell *et al.*, *Science* **335**, 947 (2012).
10. T. Georgiou *et al.*, *Nat. Nanotechnol.* **8**, 100 (2013).
11. R. V. Gorbachev *et al.*, *Nat. Phys.* **8**, 896 (2012).
12. C. R. Dean *et al.*, *Nat. Phys.* **7**, 693 (2011).
13. J. N. Coleman *et al.*, *Science* **331**, 568 (2011).
14. Q. H. Wang, K. Kalantar-Zadeh, A. Kis, J. N. Coleman, M. S. Strano, *Nat. Nanotechnol.* **7**, 699 (2012).
15. L. F. Mattheiss, *Phys. Rev. B* **8**, 3719 (1973).
16. A. Ayari, E. Cobas, O. Ogundadegbe, M. S. Fuhrer, *J. Appl. Phys.* **101**, 014507 (2007).
17. A. H. Castro Neto, *Phys. Rev. Lett.* **86**, 4382 (2001).
18. A. Kumar, P. K. Ahluwalia, *Eur. Phys. J. B* **85**, 186 (2012).
19. M. R. Hilton, P. D. Fleischauer, *Surf. Coat. Tech.* **54-55**, 435 (1992).
20. S. R. Cohen *et al.*, *Thin Solid Films* **324**, 190 (1998).
21. C. Ballif *et al.*, *Appl. Phys. A Mat. Sci. Process.* **62**, 543 (1996).
22. E. Fortin, W. M. Sears, *J. Phys. Chem. Solids* **43**, 881 (1982).
23. K. K. Kam, B. A. Parkinson, *J. Phys. Chem.* **86**, 463 (1982).
24. H. Tributsch, H. Gerischer, C. Clemen, E. Bucher, *Phys. Chem. Chem. Phys.* **83**, 655 (1979).
25. C. Lee, X. D. Wei, J. W. Kysar, J. Hone, *Science* **321**, 385 (2008).
26. A. Castellanos-Gomez *et al.*, *Nanoscale Res. Lett.* **7**, 233 (2012).
27. See supplementary materials on Science Online.
28. S. J. Haigh *et al.*, *Nat. Mater.* **11**, 764 (2012).
29. A. S. Mayorov *et al.*, *Nano Lett.* **11**, 2396 (2011).
30. A. H. Castro Neto, F. Guinea, N. M. R. Peres, K. S. Novoselov, A. K. Geim, *Rev. Mod. Phys.* **81**, 109 (2009).
31. B. E. A. Saleh, M. C. Teich, *Fundamentals of Photonics*. Wiley Series in Pure and Applied Optics (Wiley, New York, ed. 2, 2007).
32. V. V. Sobolev, V. V. Sobolev, *J. Appl. Spectrosc.* **61**, 532 (1994).
33. M. S. Dresselhaus *et al.*, *Acc. Chem. Res.* **35**, 1070 (2002).
34. B. Sachs *et al.*, Doping mechanisms in graphene-MoS₂ hybrids; arXiv:1304.2236 (2013).
35. M. Furchi *et al.*, *Nano Lett.* **12**, 2773 (2012).
36. P. Blake *et al.*, *Appl. Phys. Lett.* **91**, 063124 (2007).
37. R. V. Gorbachev *et al.*, *Small* **7**, 465 (2011).
38. S. M. Nie, S. R. Emory, *Science* **275**, 1102 (1997).
39. H. A. Atwater, A. Polman, *Nat. Mater.* **9**, 205 (2010).
40. T. J. Echtermeyer *et al.*, *Nature Communications* **2**, 458 (2011).
41. O. Hess *et al.*, *Nat. Mater.* **11**, 573 (2012).

Acknowledgments: This work was supported by the Royal Society, European Research Council, U.S. Army, EPSRC and European Science Foundation (ESF) under the EUROCORES Programme EuroGRAPHENE (GOSPEL). A.M. acknowledges support from the Swiss National Science Foundation. A.H.C.N. acknowledges support from the National Research Foundation (NRF) of Singapore through NRF-CRP award "Novel 2D materials with tailored properties: Beyond graphene" (R-144-000-295-281). Y.-J.K.'s work was supported by the Global Research Laboratory (GRL) Program (2011-0021972) of the Ministry of Education, Science and Technology, Korea. R.M.R. is thankful for the financial support of the Portuguese FCT under grant SFRH/BSAB/1249/2012.

Supplementary Materials

www.sciencemag.org/cgi/content/full/science.1235547/DC1
Materials and Methods
Supplementary Text
Figs. S1 to S9
References (42–50)

23 January 2013; accepted 18 April 2013
Published online 2 May 2013;
10.1126/science.1235547

PHYSICS

Two Two-Dimensional Materials Are Better than One

Joachim M. Hamm and Ortwin Hess

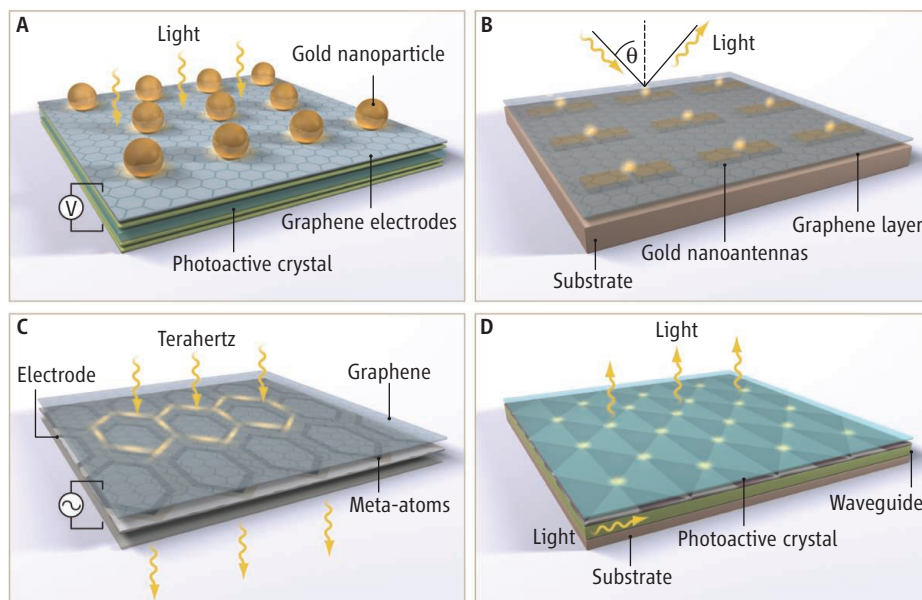
Extraordinary electronic or optical properties can result when layered solids are realized as two-dimensional (2D) materials (single or few-layer sheets), as is the case when graphene is formed from graphite. Optical properties can also be enhanced by restructuring materials at sub-wavelength scales into metamaterials, such as enhancing the plasmonic properties of gold—the coupling of light to electrons—by forming nanoparticles. Combining these approaches can lead to devices with capabilities that are otherwise difficult to realize. For example, for photovoltaic devices or sensors, materials with high electronic conductivity could be optically thick (to efficiently absorb light) but dimensionally thin (to impart flexibility and light weight). On page 1311 of this issue, Britnell *et al.* (1) combined highly conductive graphene and optically active 2D transition metal dichalcogenides into a heterostructure that photoexcites electron-hole pairs within a band-gap material. These carriers were separated with a p-n junction and extracted as a photocurrent with transparent graphene electrodes (graphene), and the performance was enhanced with plasmonic gold nanoparticles.

How does the light-matter interaction become stronger by making a particu-

lar material to become 2D, e.g., by exfoliation of single layers and making it so thin that it effectively has no thickness relative to the wavelength of light? This surprising property is directly related to the presence

Combining 2D materials and 2D metasurfaces enables the fabrication of photonic devices based on extreme interactions between electrons and light.

of critical points that generate in 2D or 1D (but not in 3D) the so-called Van Hove singularities in the electronic structure. Britnell *et al.* report that for the photoactive transition metal dichalcogenides such as molybdenum



Uniting flat materials. Various ultraflat photonic devices that could be built through the combination of 2D electronic materials and 2D photonic metasurfaces are illustrated. (A) Ultrathin broadband photovoltaic devices could be realized by combining 2D materials and broadband light harvesting (1). (B) Label-free single-molecule detectors could be achieved by exploiting a diffractive coupling between plasmonic nanoantennas functionalized by a graphene layer (10). (C) A polarization-independent terahertz modulator could be made by using gate-tunable graphene embedded in a metamaterial structure (11). (D) Ultrafast and broadband metasurface emitters could be made by tailoring the 2D active material to operate in visible light or in the terahertz regime (8, 12).

The Blackett Laboratory, Department of Physics, Imperial College London, London SW7 2AZ, UK. E-mail: j.hamm@imperial.ac.uk; o.hess@imperial.ac.uk

disulfide (MoS₂), these singularities occur at visible frequencies and enhance the electronic density of states, i.e., the number of electrons per volume that participate in the absorption process at a given energy. Using this fundamental concept, a remarkably high quantum efficiency of up to 30% was achieved experimentally, in part by adding layers of hexagonal boron nitrate to provide homogenization of the doping levels.

The light-matter interaction was further increased by manipulating the local optical density of states. Britnell *et al.* show that depositing gold nanoparticles on the surface of the 2D heterostructure further enhanced the photogeneration of electron-hole pairs by a factor of 10. The nanoplasmonic particles form a broadband light-harvesting metamaterial (2) that concentrates field energy (or bundles optical modes) in “hotspots” under the particles. Additional generation of carri-

ers takes place where these hotspots overlap with the photoactive layer.

These results not only demonstrate that the simultaneous design of the electronic and the optical density of states is the key to an extreme control of light-matter interaction but also provide a glimpse of how future nanophotonic devices can benefit from the combination of two 2D materials: heterostructures of 2D atomic crystals (“electronic metamaterials”) to control the electronic wave functions and nanostructured metasurfaces (3–5) to control the light field. This principle, which we call the “United Flatlands” (6, 7) opens up many opportunities for the next generation of active 2D metamaterials (8) with quantum gain (9) and ultraflat photonic devices, such as solar cells, light-emitting diodes, nanolasers, and optical sensors. The figure showcases some of the most striking possibilities. With the potential to break many performance and

size limitations of bulk materials, particularly with respect to speed, energy efficiency, and area-footprint, the marriage of electronic and optical 2D (meta-) materials heralds a quantum leap in photonic device technology.

References and Notes

1. L. Britnell *et al.*, *Science* **340**, 1311 (2013).
2. J. B. Pendry *et al.*, *Science* **337**, 549 (2012).
3. N. Yu *et al.*, *Nano Lett.* **12**, 6328 (2012).
4. X. Yin *et al.*, *Science* **339**, 1405 (2013).
5. A. V. Kildishev *et al.*, *Science* **339**, 1289 (2013).
6. A. K. Geim, A. H. MacDonald, *Phys. Today* **60**, 35 (2007).
7. O. Hess, *Nature* **455**, 299 (2008).
8. O. Hess *et al.*, *Nat. Mater.* **11**, 573 (2012).
9. O. Hess, K. L. Tsakmakidis, *Science* **339**, 654 (2013).
10. V. G. Kravets *et al.*, *Nat. Mater.* **12**, 304 (2013).
11. S. H. Lee *et al.*, *Nat. Mater.* **11**, 936 (2012).
12. P. M. Z. Davies *et al.*, arXiv:1305.2839 (2013).

Acknowledgments: Supported by the Leverhulme Trust and the Engineering and Physical Sciences Research Council.

10.1126/science.1239501



Supplementary Materials for

Strong Light-Matter Interactions in Heterostructures of Atomically Thin Films

L. Britnell, R. M. Ribeiro, A. Eckmann, R. Jalil, B. D. Belle, A. Mishchenko, Y.-J. Kim,
R. V. Gorbachev, T. Georgiou, S. V. Morozov, A. N. Grigorenko, A. K. Geim,
C. Casiraghi, A. H. Castro Neto,* K. S. Novoselov

*Corresponding author. E-mail: phycastr@nus.edu.sg

Published 2 May 2013 on *Science Express*
DOI: 10.1126/science.1235547

This PDF file includes:

Materials and Methods
Supplementary Text
Figs. S1 to S9
References

Device preparation

Graphene and thin graphite flakes were produced by micromechanical exfoliation of graphite. We used single crystal WS₂ supplied in powder form by Sigma-Aldrich. Despite an average crystal size of only 2 μm it is possible to find crystals up to 50 μm that could be exfoliated as well.

Recent progress has led to relatively facile fabrication of graphene hybrid devices with a large degree of versatility (7-9). The method allows flakes of layered materials to be transferred to the surfaces of one another with a high degree of accuracy and cleanliness. In this way, stacks of different materials can be created with precise control over the constituents of the new hybrid material.

We have used a so-called ‘dry’ transfer technique (7, 8) to create these structures. This technique involves the mechanical exfoliation of the required flakes onto a dual layer polymer stack. The bottom polymer layer can be selectively dissolved and the resulting membrane inverted and positioned above the target flake—the initial bottom flake was instead cleaved onto a Si/SiO₂ wafer (290 nm oxide). After each transfer the top polymer layer was dissolved and the device annealed thoroughly in a gaseous mixture of H₂/Ar (10:90) at 250 °C before the subsequent transfer of the next flake. In this way stacks with an arbitrary number of layers can be produced. Once the required flake stack had been fabricated, electrical contact was made via standard photolithographic processing and e-beam evaporation of a Cr adhesion layer (5nm) and Au (50 nm) and placed in a package for measurements. In order to make scanning photocurrent microscopy measurements we utilize a WITec scanning Raman system. The sample was placed onto a piezoelectric stage with laser light incident from above. The laser was focused by a 100x microscope objective with a laser spot size that is diffraction limited (diameter ~500 nm). The laser spot is scanned over the surface and the resultant current flow between the two graphene electrodes is measured simultaneously with the Raman spectra for each point in the scan.

We used chemical vapour deposition (CVD) to fabricate high-quality, large area graphene electrodes. The graphene was grown on 25 μm thick copper (Cu) foil (from Alfa Aesar, item no. 13382). Before graphene deposition, the Cu foils were cleaned with subsequent washes in acetone, DI water and IPA in order to remove both organic and inorganic contamination from the surface. To further improve the CVD graphene quality and increase grain size, the Cu foil was then annealed in a quartz tube for 30 minutes at 1000 °C in a flux of H₂ at 20 sccm and chamber pressure 200 mTorr. Graphene was grown on the Cu surface by adding 40 sccm CH₄ to the gas flow (chamber pressure fixed at 600 mTorr) whilst maintaining a temperature of

1000 °C. The sample was allowed to cool in a H₂ atmosphere and then removed from the chamber at room temperature. The graphene could then be transferred to a silicon wafer by etching of the Cu foil. Details of the transfer procedure are given in ref (42).

Examples of device operation with molybdenum disulfide (MoS₂)

The manuscript focuses on the most efficient devices that we measured which were fabricated with WS₂ as the semiconducting region. However, the results apply universally to all the transition metal dichalcogenides. Here we show that a similar behaviour was observed with MoS₂. The devices were fabricated in the same fashion as described above. To summarise, the devices consist of a tri-layer structure comprising a TMDC flake sandwiched between two electrically isolated graphene layers which act as transparent electrodes. The device sits on an oxidised silicon wafer with the doped silicon acting as a gate electrode. The electric field across the semiconducting region can be altered by applying a voltage between the bottom graphene layer and the doped silicon back gate.

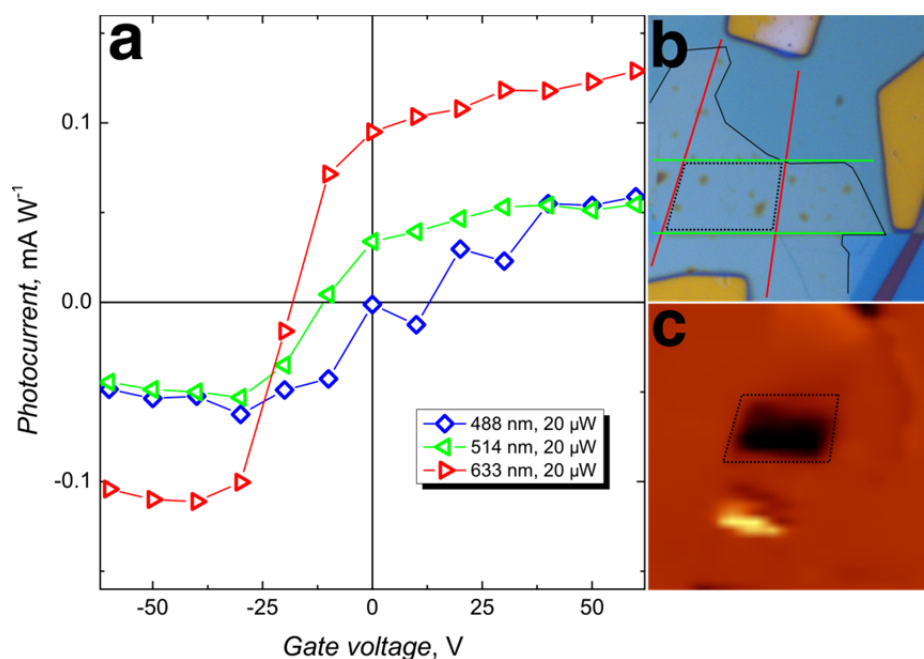


Figure S1 MoS₂ photovoltaic device. **a** The photocurrent of a MoS₂ device as a function of gate voltage for three laser lines: red – 633 nm, green – 514 nm and blue – 488 nm. The device was fabricated on an oxidised silicon wafer (300 nm thick thermally grown oxide – IDB Technologies) with a BN substrate (~30 nm thick) flake. The current flow between the two graphene layers was recorded as a function of the laser spot position as it was raster scanned across the surface. The data points shown are the average values taken from photocurrent maps taken at each gate voltage (shown in panel **c**). **b** An optical image of the device where the top (bottom) graphene layer is outlined in green (red) and the MoS₂ flake is outlined by the solid black line. **c** A photocurrent map taken at V_g = -60 V. The region over which the average photocurrent signal was measured is shown by the dotted outline. This corresponds to the same area shown in **b**.

The efficiency of our devices fabricated with MoS₂ was found to be lower than for WS₂. This is unexpected from the calculated DOS which are similar for all the TMDCs but it is speculated that a higher level of impurity atoms such as rhenium present in the MoS₂ lattice could be responsible due to creation of impurity states in the band gap which increase the rate of recombination.

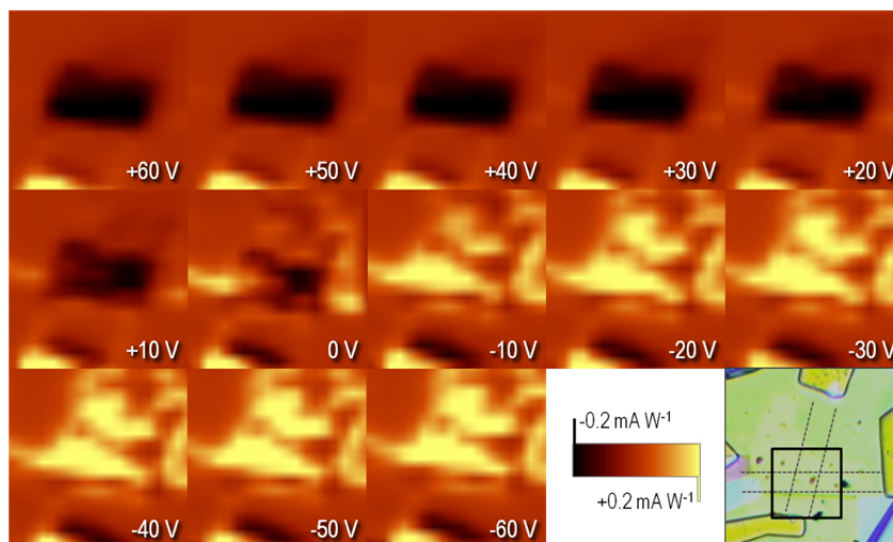


Figure S2 Photocurrent maps of a MoS₂ device. Photocurrent maps recorded over a range of gate voltages from -60 to + 60 V. The electric field due to the back gate tunes the sign and magnitude of the photocurrent signal. The region shown in the maps is indicated by the back square shown in the optical image in the bottom right hand panel where the outline of the graphene layers is also indicated by the dashed black lines.

Examples of device operation with GaSe

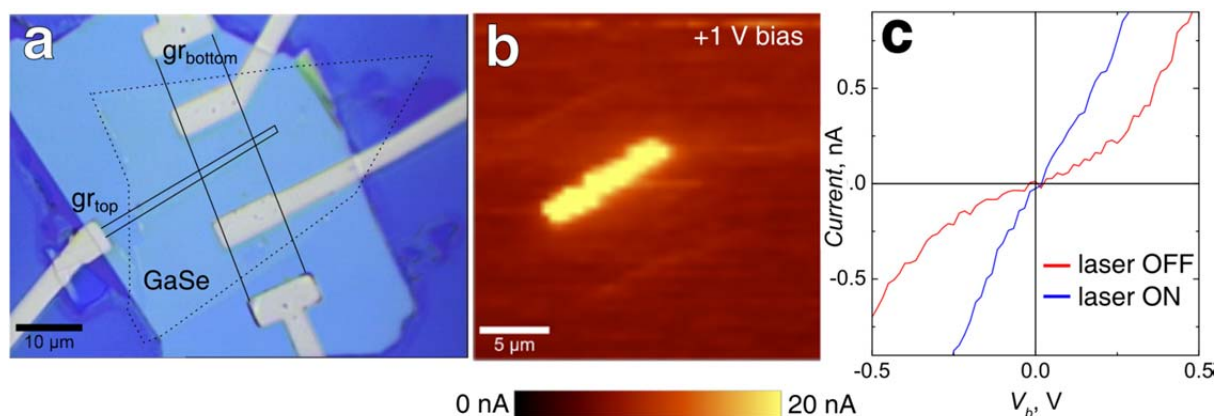


Figure S3 Photocurrent maps of a GaSe device. **a.** Optical image of a GaSe device with top and bottom graphene contacts as labelled on the image. The outlines of the various component materials are drawn due to the lack of optical contrast. **b.** A photocurrent map recorded with a +1 V bias between the graphene electrodes due to the high resistance of the device. The region shown is centred on the active region where the bright area is the overlap top and bottom graphene electrodes with the GaSe crystal. **c** *IV* curves taken on the device with and without laser illumination on the active region. The laser was 2.54 eV at an intensity of 90 mW

Figure S3 shows the optical and corresponding photocurrent map of a GaSe device. The efficiency was found to be lower than for WS₂ but qualitatively the same behaviour was observed. As expected the illumination with visible wavelength laser light led to a decrease in the resistivity of the device.

Power dependent *IV* curves for WS₂

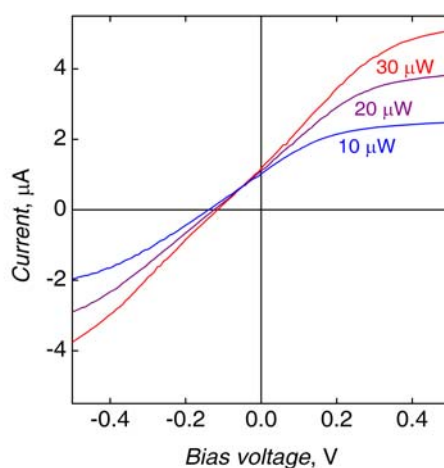


Figure S4 Photoresistivity. *IV* characteristics of the device shown in fig 2, under laser illumination of varying intensity. The resistivity of the device changes only when laser light is incident on the region where all three constituent flakes overlap and the slope of the *IV* curves is dependent on the power. Shown are *IV* curves taken with a 2.54 eV laser set to a total power of 10, 20 and 30 μW , all at $V_g = -20$ V. The *IV* curve without illumination is too small to see on this scale but one can compare with fig. 2 of the main text.

Three *IV* curves taken at different power's showing the photo-resistivity dependent on illumination intensity. The saturation current (at higher bias) is proportional to intensity.

Plasmonic enhancement

The already good performance and high EQE of our devices (ensured by the peculiar band structure of TMDC used) can be further improved by optimizing light absorption in the active layer. However, the simplest strategy of increasing the thickness of TMDC layer might not be the optimum one, since the internal electric field (which dissociate the electron-hole pairs) decreases as the thickness increases, and also other recombination channels might become more effective, thus reducing the photocurrent. Alternative ways to boost the light adsorption are the use of optical resonators (35) or plasmonic enhancement of light absorption (38-40). The further is already partly realized in our devices on SiO₂, where light interference in SiO₂

layer (36, 37) enhances the optical electric field in TMDC (this is one of the reasons of better performance of our devices on SiO₂ in comparison with those on flexible substrates).

The latter strategy of utilization plasmonic nanostructures (38-40) or metamaterials (41) allows even more freedom. One can use metal nanoparticles to generate evanescent photons in near-field under light illumination. The proximity to TMDC layer leads to adsorption of such near-field photons in the active layer with very high efficiency, due to specific confinement of such photons(43). We tested this idea on several of our MoS₂ by spattering thin layer of gold, which, after successive annealing coagulate into droplets of 5-10nm in height. It has been shown previously, that such strategy allows for a significant enhancement of the Raman signal in graphene(44). Here we observed 10-fold increase of the photocurrent signal after introduction of such plasmonic nanostructures, proving that this strategy is a viable route of pushing the EQE of such heterostructures even higher (Fig. S5).

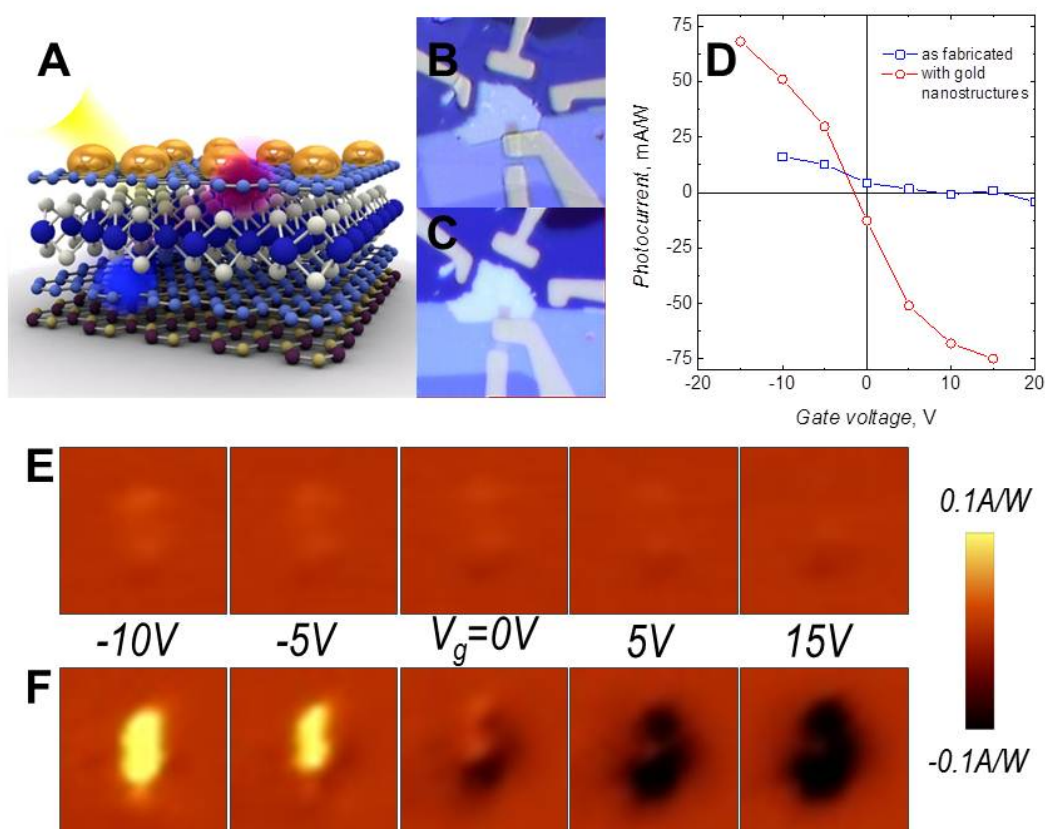


Figure S5 Plasmonic enhancement. (A) Schematic representation of hBN/Gr/MoS₂/Gr device with gold nano-dots on top. (B-C) Optical photograph of one of such device before (B) and after (C) deposition of nano-dots. The size of the images is 50μm×50μm. (D) Dependence of photocurrent on gate voltage. Each point is the average photocurrent over the active area of device. (E-F) Maps of photocurrent as the focused laser beam scans across the active area of device with (F) and without (E) golden nano-dots. The size of each map is 14μm×14μm.

DFT calculations

The density functional calculations were performed using the open source code Quantum Espresso (45). We performed full relativistic calculations with spin-orbit. The exchange correlation energy was described by the generalized gradient approximation (GGA), in the scheme proposed by Perdew-Burke-Ernzerhof (46) (PBE) and a semi-empirical dispersion term (47, 48) (DFT-D) was applied.

The Brillouin-zone (BZ) was sampled for integrations according to the scheme proposed by Monkhorst–Pack (49). A grid of 16x16x16 \mathbf{k} -points was used for the bulk samples and a grid of 16x16x1 \mathbf{k} -points for the single layer samples. An increase in the number of points did not result in a significant total energy change. The energy cut-off was 150 Ry. An increase in the energy cut-off did not result in a significant total energy change.

We used norm conserving, full relativistic pseudopotentials with nonlinear core-correction to describe the ion cores. The W pseudopotential was produced with 6s2 5d4 electrons in the valence band, Mo with 5s1 4d5 electrons, and S and Se with $ns2 np4$ electrons in the valence band.

Single layer samples were modeled in a slab geometry by including a vacuum region of 45 Bohr in the direction perpendicular to the surface. The lattice parameters were also relaxed, at the same time as the atoms positions. In the calculations, all the atoms were fully relaxed to their equilibrium positions until there were no forces larger than 0.005 eV/Å.

The electronic density of states was calculated by sampling 17576 points in the BZ for the bulk samples and 3888 in the single layers, and broadened with a 0.01 eV Gaussian width. The tetrahedron method (50) was used.

The equation used to calculate JDoS(E) is given in the main text. A Gaussian broadening of 0.04 eV width was applied.

The continuum energy was determined in the three single layer samples by calculating the total electric potential along the normal to the surface, and taking the value when the potential becomes constant. For the bulk samples, the difference in energy between the lowest energy bands of the bulk and single layer was determined. These bands are sufficiently low in energy that are not much affected by the environment, and keep essentially the same shape in bulk and single layer (except for the factor of 2 resulting from the bulk having twice as many atoms in the unit cell). Figure S6 shows the electronic density of states of the deep bands used to calculate the continuum energy; it can be seen that the shape of these bands are very

similar in the bulk and the single layer. The main differences come from the fact that in the single layer the spin orbit interaction barely removes the degeneracy, while in the bulk it does (see figure S7).

Figure S7 shows the band structure of WSe₂ both in bulk and single layer. The zero energy is aligned with the vacuum energy. The notation of the symmetry points is the standard, and is depicted in figure S8.

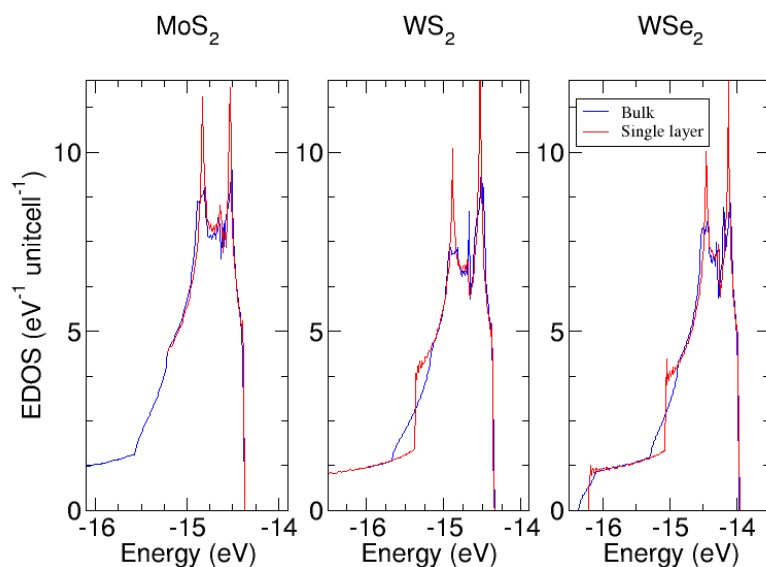


Figure S6: The electronic density of states of deep bands used to calculate the continuum energy of bulk samples. The single layer density of states were multiplied by two to show the superposition of the bands more clearly.

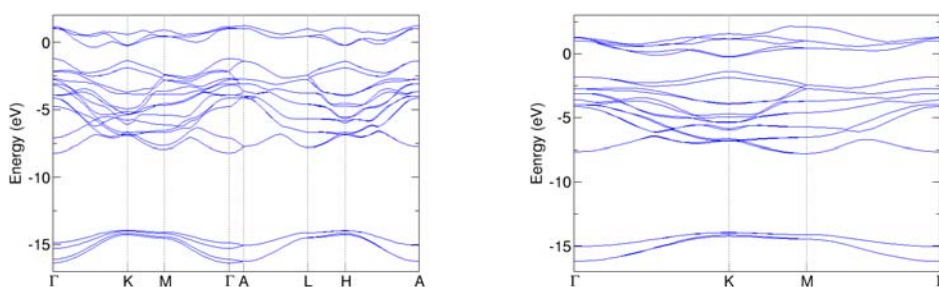


Figure S7: The band structure of bulk (left) and single layer (right) of WSe₂

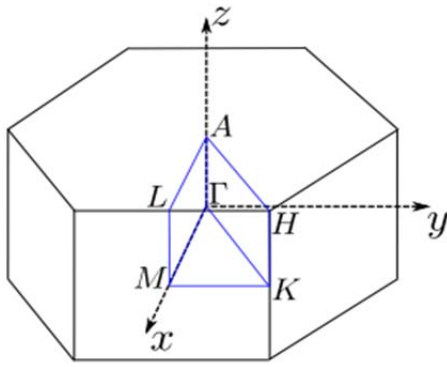


Figure S8: The Brillouin zone for the hexagonal lattice, with the symmetry points.

DFT calculations for bulk TMDC

In order to further confirm that our results are not dependent on the thickness of the TMDC, we calculated the DoS and JDoS for bulk (3D) semiconducting TMDCs. The sharp peaks in the DoS and the sharp rise of the JDoS is comparable with the values found for a single layer in Fig.3B. Hence, the strong light-matter interactions in semiconducting TMDCs is not a unique feature of the bulk material and it can be extended to monolayers.

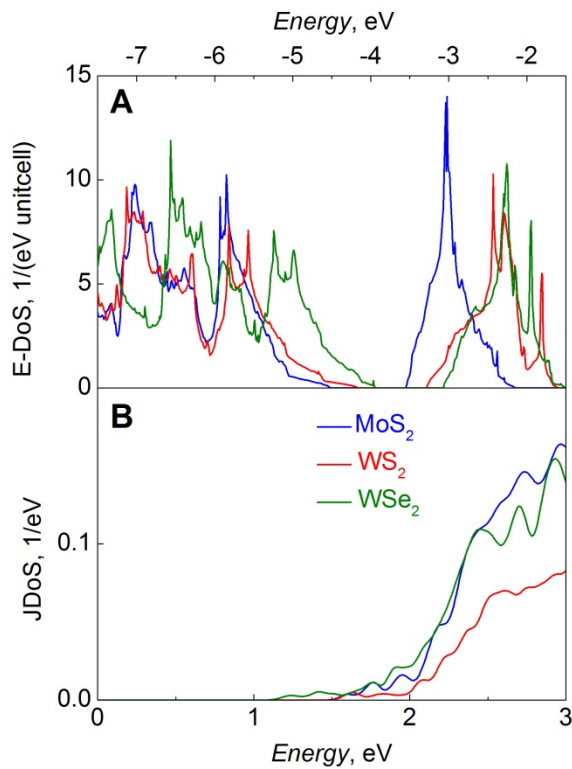


Figure S9: Electronic DoS for bulk TMDCs.

(A) The DoS for bulk TMDCs: MoS₂, WS₂ and WSe₂. Similar to the single layer case strong peaks are again present. (B) The JDoS with the same three TMDC materials again showing a sharp rise in the visible range.

References

1. K. S. Novoselov *et al.*, Electric field effect in atomically thin carbon films. *Science* **306**, 666 (2004). [doi:10.1126/science.1102896](https://doi.org/10.1126/science.1102896) [Medline](#)
2. A. K. Geim, K. S. Novoselov, The rise of graphene. *Nat. Mater.* **6**, 183 (2007). [doi:10.1038/nmat1849](https://doi.org/10.1038/nmat1849) [Medline](#)
3. A. K. Geim, Graphene: status and prospects. *Science* **324**, 1530 (2009). [doi:10.1126/science.1158877](https://doi.org/10.1126/science.1158877) [Medline](#)
4. A. K. Geim, Nobel Lecture: Random walk to graphene. *Rev. Mod. Phys.* **83**, 851 (2011). [doi:10.1103/RevModPhys.83.851](https://doi.org/10.1103/RevModPhys.83.851)
5. K. S. Novoselov, Nobel Lecture: Graphene: Materials in the Flatland. *Rev. Mod. Phys.* **83**, 837 (2011). [doi:10.1103/RevModPhys.83.837](https://doi.org/10.1103/RevModPhys.83.837)
6. K. S. Novoselov *et al.*, Two-dimensional atomic crystals. *Proc. Natl. Acad. Sci. U.S.A.* **102**, 10451 (2005). [doi:10.1073/pnas.0502848102](https://doi.org/10.1073/pnas.0502848102) [Medline](#)
7. C. R. Dean *et al.*, Boron nitride substrates for high-quality graphene electronics. *Nat. Nanotechnol.* **5**, 722 (2010). [doi:10.1038/nnano.2010.172](https://doi.org/10.1038/nnano.2010.172) [Medline](#)
8. L. A. Ponomarenko *et al.*, Tunable metal-insulator transition in double-layer graphene heterostructures. *Nat. Phys.* **7**, 958 (2011). [doi:10.1038/nphys2114](https://doi.org/10.1038/nphys2114)
9. L. Britnell *et al.*, Field-effect tunneling transistor based on vertical graphene heterostructures. *Science* **335**, 947 (2012). [doi:10.1126/science.1218461](https://doi.org/10.1126/science.1218461) [Medline](#)
10. T. Georgiou *et al.*, Vertical field-effect transistor based on graphene-WS₂ heterostructures for flexible and transparent electronics. *Nat. Nanotechnol.* **8**, 100 (2013). [doi:10.1038/nnano.2012.224](https://doi.org/10.1038/nnano.2012.224) [Medline](#)
11. R. V. Gorbachev *et al.*, Strong Coulomb drag and broken symmetry in double-layer graphene. *Nat. Phys.* **8**, 896 (2012). [doi:10.1038/nphys2441](https://doi.org/10.1038/nphys2441)
12. C. R. Dean *et al.*, Multicomponent fractional quantum Hall effect in graphene. *Nat. Phys.* **7**, 693 (2011). [doi:10.1038/nphys2007](https://doi.org/10.1038/nphys2007)
13. J. N. Coleman *et al.*, Two-dimensional nanosheets produced by liquid exfoliation of layered materials. *Science* **331**, 568 (2011). [doi:10.1126/science.1194975](https://doi.org/10.1126/science.1194975) [Medline](#)
14. Q. H. Wang, K. Kalantar-Zadeh, A. Kis, J. N. Coleman, M. S. Strano, Electronics and optoelectronics of two-dimensional transition metal dichalcogenides. *Nat. Nanotechnol.* **7**, 699 (2012). [doi:10.1038/nnano.2012.193](https://doi.org/10.1038/nnano.2012.193) [Medline](#)
15. L. F. Mattheiss, Band structures of transition-metal-dichalcogenide layer compounds. *Phys. Rev. B* **8**, 3719 (1973). [doi:10.1103/PhysRevB.8.3719](https://doi.org/10.1103/PhysRevB.8.3719)
16. A. Ayari, E. Cobas, O. Ogundadegbe, M. S. Fuhrer, Realization and electrical characterization of ultrathin crystals of layered transition-metal dichalcogenides. *J. Appl. Phys.* **101**, 014507 (2007). [doi:10.1063/1.2407388](https://doi.org/10.1063/1.2407388)
17. A. H. Castro Neto, Charge density wave, superconductivity, and anomalous metallic behavior in 2D transition metal dichalcogenides. *Phys. Rev. Lett.* **86**, 4382 (2001). [doi:10.1103/PhysRevLett.86.4382](https://doi.org/10.1103/PhysRevLett.86.4382) [Medline](#)

18. A. Kumar, P. K. Ahluwalia, Electronic structure of transition metal dichalcogenides monolayers 1H-MX₂ (M = Mo, W; X = S, Se, Te) from ab-initio theory: New direct band gap semiconductors. *Eur. Phys. J. B* **85**, 186 (2012). [doi:10.1140/epjb/e2012-30070-x](https://doi.org/10.1140/epjb/e2012-30070-x)
19. M. R. Hilton, P. D. Fleischauer, Applications of solid lubricant films in spacecraft. *Surf. Coat. Tech.* **54-55**, 435 (1992). [doi:10.1016/S0257-8972\(07\)80062-4](https://doi.org/10.1016/S0257-8972(07)80062-4)
20. S. R. Cohen *et al.*, The tribological behavior of type II textured MX₂ (M=Mo, W; X=S, Se) films. *Thin Solid Films* **324**, 190 (1998). [doi:10.1016/S0040-6090\(97\)01218-2](https://doi.org/10.1016/S0040-6090(97)01218-2)
21. C. Ballif *et al.*, *Appl. Phys. A Mat. Sci. Process.* **62**, 543 (1996).
22. E. Fortin, W. M. Sears, Photovoltaic effect and optical absorption in MoS₂. *J. Phys. Chem. Solids* **43**, 881 (1982). [doi:10.1016/0022-3697\(82\)90037-3](https://doi.org/10.1016/0022-3697(82)90037-3)
23. K. K. Kam, B. A. Parkinson, Detailed photocurrent spectroscopy of the semiconducting group VIB transition metal dichalcogenides. *J. Phys. Chem.* **86**, 463 (1982). [doi:10.1021/j100393a010](https://doi.org/10.1021/j100393a010)
24. H. Tributsch, H. Gerischer, C. Clemen, E. Bucher, Berichte Der Bunsen-Gesellschaft-. *Phys. Chem. Chem. Phys.* **83**, 655 (1979).
25. C. Lee, X. D. Wei, J. W. Kysar, J. Hone, Measurement of the elastic properties and intrinsic strength of monolayer graphene. *Science* **321**, 385 (2008). [doi:10.1126/science.1157996](https://doi.org/10.1126/science.1157996) [Medline](#)
26. A. Castellanos-Gomez *et al.*, Mechanical properties of freely suspended semiconducting graphene-like layers based on MoS₂. *Nanoscale Res. Lett.* **7**, 233 (2012). [doi:10.1186/1556-276X-7-233](https://doi.org/10.1186/1556-276X-7-233) [Medline](#)
27. See supplementary materials on *Science Online*.
28. S. J. Haigh *et al.*, Cross-sectional imaging of individual layers and buried interfaces of graphene-based heterostructures and superlattices. *Nat. Mater.* **11**, 764 (2012). [doi:10.1038/nmat3386](https://doi.org/10.1038/nmat3386) [Medline](#)
29. A. S. Mayorov *et al.*, Micrometer-scale ballistic transport in encapsulated graphene at room temperature. *Nano Lett.* **11**, 2396 (2011). [doi:10.1021/nl200758b](https://doi.org/10.1021/nl200758b) [Medline](#)
30. A. H. Castro Neto, F. Guinea, N. M. R. Peres, K. S. Novoselov, A. K. Geim, The electronic properties of graphene. *Rev. Mod. Phys.* **81**, 109 (2009). [doi:10.1103/RevModPhys.81.109](https://doi.org/10.1103/RevModPhys.81.109)
31. B. E. A. Saleh, M. C. Teich, *Fundamentals of Photonics*. Wiley Series in Pure and Applied Optics (Wiley, New York, ed. 2, 2007).
32. V. V. Sobolev, V. V. Sobolev, Optical spectra of molybdenum disulfide in the region between 1 and 30 eV. *J. Appl. Spectrosc.* **61**, 532 (1994). [doi:10.1007/BF02606398](https://doi.org/10.1007/BF02606398)
33. M. S. Dresselhaus *et al.*, Single nanotube Raman spectroscopy. *Acc. Chem. Res.* **35**, 1070 (2002). [doi:10.1021/ar0101537](https://doi.org/10.1021/ar0101537) [Medline](#)
34. B. Sachs *et al.*, Doping mechanisms in graphene-MoS₂ hybrids; arXiv:1304.2236 (2013).
35. M. Furchi *et al.*, Microcavity-integrated graphene photodetector. *Nano Lett.* **12**, 2773 (2012). [doi:10.1021/nl204512x](https://doi.org/10.1021/nl204512x) [Medline](#)

36. P. Blake *et al.*, Making graphene visible. *Appl. Phys. Lett.* **91**, 063124 (2007).
[doi:10.1063/1.2768624](https://doi.org/10.1063/1.2768624)
37. R. V. Gorbachev *et al.*, Hunting for monolayer boron nitride: Optical and Raman signatures. *Small* **7**, 465 (2011). [doi:10.1002/sml.201001628](https://doi.org/10.1002/sml.201001628) [Medline](#)
38. S. M. Nie, S. R. Emory, Probing single molecules and single nanoparticles by surface-enhanced Raman scattering. *Science* **275**, 1102 (1997).
[doi:10.1126/science.275.5303.1102](https://doi.org/10.1126/science.275.5303.1102) [Medline](#)
39. H. A. Atwater, A. Polman, Plasmonics for improved photovoltaic devices. *Nat. Mater.* **9**, 205 (2010). [doi:10.1038/nmat2629](https://doi.org/10.1038/nmat2629) [Medline](#)
40. T. J. Echtermeyer *et al.*, Strong plasmonic enhancement of photovoltage in graphene. *Nature Communications* **2**, 458 (2011). [doi:10.1038/ncomms1464](https://doi.org/10.1038/ncomms1464) [Medline](#)
41. O. Hess *et al.*, Active nanoplasmonic metamaterials. *Nat. Mater.* **11**, 573 (2012).
[doi:10.1038/nmat3356](https://doi.org/10.1038/nmat3356) [Medline](#)
42. S. Bae *et al.*, Roll-to-roll production of 30-inch graphene films for transparent electrodes. *Nat. Nanotechnol.* **5**, 574 (2010). [doi:10.1038/nnano.2010.132](https://doi.org/10.1038/nnano.2010.132) [Medline](#)
43. F. Schedin *et al.*, Surface-enhanced Raman spectroscopy of graphene. *ACS Nano* **4**, 5617 (2010). [doi:10.1021/nn1010842](https://doi.org/10.1021/nn1010842) [Medline](#)
44. J. Lee, K. S. Novoselov, H. S. Shin, Interaction between metal and graphene: dependence on the layer number of graphene. *ACS Nano* **5**, 608 (2011). [doi:10.1021/nn103004c](https://doi.org/10.1021/nn103004c) [Medline](#)
45. P. Giannozzi *et al.*, Quantum Espresso: A modular and open-source software project for quantum simulations of materials. *J. Phys. Condens. Matter* **21**, 395502 (2009).
[doi:10.1088/0953-8984/21/39/395502](https://doi.org/10.1088/0953-8984/21/39/395502) [Medline](#)
46. J. P. Perdew, K. Burke, M. Ernzerhof, Generalized gradient approximation made simple [Phys. Rev. Lett. 77, 3865 (1996)]. *Phys. Rev. Lett.* **78**, 1396 (1997).
[doi:10.1103/PhysRevLett.78.1396](https://doi.org/10.1103/PhysRevLett.78.1396)
47. S. Grimme, Semiempirical GGA-type density functional constructed with a long-range dispersion correction. *J. Comput. Chem.* **27**, 1787 (2006). [doi:10.1002/jcc.20495](https://doi.org/10.1002/jcc.20495) [Medline](#)
48. V. Barone *et al.*, Role and effective treatment of dispersive forces in materials: Polyethylene and graphite crystals as test cases. *J. Comput. Chem.* **30**, 934 (2009).
[doi:10.1002/jcc.21112](https://doi.org/10.1002/jcc.21112) [Medline](#)
49. H. J. Monkhorst, J. D. Pack, Special points for Brillouin-zone integrations. *Phys. Rev. B* **13**, 5188 (1976). [doi:10.1103/PhysRevB.13.5188](https://doi.org/10.1103/PhysRevB.13.5188)
50. P. E. Blöchl, O. Jepsen, O. K. Andersen, Improved tetrahedron method for Brillouin-zone integrations. *Phys. Rev. B* **49**, 16223 (1994). [doi:10.1103/PhysRevB.49.16223](https://doi.org/10.1103/PhysRevB.49.16223) [Medline](#)